PAPER

Identifying surface structural changes in layered Li-excess nickel manganese oxides in high voltage lithium ion batteries: A joint experimental and theoretical study†

Bo Xu,‡[a] Christopher R. Fell,‡[b] Miaofang Chi[c] and Ying Shirley Meng*[ab]

High voltage cathode materials Li-excess layered oxide compounds $Li[Ni_xLi_{1/3-2x/3}Mn_{2/3-x/3}]O_2$ $(0 < x < 1/2)$ are investigated in a joint study combining both computational and experimental methods. The bulk and surface structures of pristine and cycled samples of $Li[Ni_{1/5}Li_{1/5}Mn_{3/5}]O_2$ are characterized by synchrotron X-Ray diffraction together with aberration corrected Scanning Transmission Electron Microscopy (a-S/TEM). Electron Energy Loss Spectroscopy (EELS) is carried out to investigate the surface changes of the samples before/after electrochemical cycling. Combining first principles computational investigation with our experimental observations, a detailed lithium de-intercalation mechanism is proposed for this family of Li-excess layered oxides. The most striking characteristics in these high voltage high energy density cathode materials are 1) formation of tetrahedral lithium ions at voltage less than 4.45 V and 2) the transition metal (TM) ions migration leading to phase transformation on the surface of the materials. We show clear evidence of a new spinel-like solid phase formed on the surface of the electrode materials after high-voltage cycling. It is proposed that such surface phase transformation is one of the factors contributing to the first cycle irreversible capacity and the main reason for the *intrinsic* poor rate capability of these materials.

[a] *Department of NanoEngineering, University of California San Diego, La Jolla, CA, 92037, USA. E-mail: shirleymeng@ucsd.edu*
[b] *Department of Materials Science and Engineering, University of Florida, Gainesville, FL, 32611, USA*
[c] *Materials Science and Technology Division, Oak Ridge National Laboratory, Oak Ridge, TN, USA*

† Electronic supplementary information (ESI) available: Rietveld refinement of the high resolution synchrotron X-ray diffraction of pristine $Li[Ni_{1/5}Li_{1/5}Mn_{3/5}]O_2$; Cation arrangements and energies of all the calculated models of $Li[Ni_{1/4}Li_{1/6}Mn_{7/12}]O_2$; The projected DOS of Mn ions in $Li_{n/12}Ni_{1/4}Mn_{7/12}O_2$ $(n = 14, 8, 0)$. See DOI: 10.1039/c1ee01131f

‡ These two authors contributed equally.

Introduction

The rechargeable Lithium Ion Battery (LIB) is one of the most important energy storage technologies today. Layered transition metal oxides, based on either $LiCoO_2$ or $LiNiO_2$ are currently used in portable electronic devices due to their high operating voltage and high specific capacity 140–160 mAh/g. To enable LIB as the main on-board storage technology in plug-in hybrid electric vehicles (PHEVs) or electric vehicles (EVs), higher energy density materials such as the "Li-excess" layered oxides, formed as the composites between $Li[Li_{1/3}Mn_{2/3}]O_2$ and $LiMO_2$ (M = Ni, Mn, Co), are promising candidates as they offer much higher capacity (>250 mAh/g) and better safety with much reduced cost.[1–3] It is now well known that in the bulk of the pristine

Broader context

High voltage high energy density Li-excess layered oxide compounds are one of the most promising candidate cathode materials used in lithium ion batteries (LIB) for on-board storage technology in plug-in hybrid electric vehicles (PHEVs) or electric vehicles (EVs). Low rate capability and large first-cycle irreversible capacity have been preventing their commercial application. In this work, the mechanisms of cation migration and subsequent surface phase transformation are described in details at the atomistic level by combining first principles computation with synchrotron X-ray diffraction (XRD), aberration corrected scanning transmission electron microscopy (a-STEM) imaging and electron energy loss spectroscopy (EELS). Stable electrode/electrolyte interface is one of the key components in designing new high energy density electrode materials for energy storage. Our research findings provide significantly new insights on understanding the complex surface chemistry in oxide materials for energy storage in LIB.

materials, the excess Li^+ ions form an ordered pattern with Mn^{4+} ions in the transition metal (TM) layer, with most of the Li surrounded by 5 or 6 Mn ions.[4–6] During the initial charging region, the capacity originates from the oxidation of Ni^{2+} to Ni^{4+} up to 4.4 V. A high voltage plateau region up to 4.8V appears after that and the anomalous high capacities have been attributed either to an irreversible loss of oxygen from the lattice during the first charge accompanied by Li removal,[3,7,8] or to the surface reaction through electrode/electrolyte reduction and/or hydrogen exchange.[5,9] Although a clear explanation of the source of the additional capacity is still under debate, previous work consistently showed that the Li/Mn ordering disappeared upon electrochemical cycling to 4.8 V, indicating significant cation rearrangement in the bulk of the materials. Armstrong *et al.* has proposed a general mechanism involving the migration of transition metal ions from surface to bulk during cycling,[7] while Jiang *et al.* provided evidence suggesting that a second phase may be generated in the high voltage region.[5] It is also shown that the lithium chemical diffusion coefficient was lowered significantly at the plateau region, as the result of this dynamic cation rearrangement.[10] The structural changes in the bulk are believed to happen mainly during the first charge since the plateau does not re-appear in the subsequent cycles. Nevertheless, the large first cycle irreversible capacity and the inferior rate capability of these materials are hindering the commercial application of these materials.

Much research efforts have been devoted to address these two issues. The most promising approaches for reducing the irreversible capacity loss involve surface coating of the cathode surface with other oxides or fluorides like Al_2O_3, $AlPO_4$ and AlF_3.[11,12] The exact mechanisms for the surface coating are still not well understood. Wu and Manthiram proposed that the reduction in irreversible capacity loss by surface coating was attributed to the retention of part of the oxygen ion vacancies in the lattice upon first charge.[12] Our recent investigation on uncoated pristine $Li[Li_{1/3-2x/3}Ni_xMn_{2/3-x/3}]O_2$ revealed that the reversible discharge capacity was affected by the surface characteristics of as-synthesized material.[10] Even without any coating, the first cycle irreversible capacity could be significantly reduced by controlling the precursor chemistry: If the surface adsorbed –OH group can be eliminated, the irreversible capacity is less than 40 mAh/g without any surface coating.[10] The low rate capability of the pristine material was proposed to be a possible result from the formation of a thick amorphous solid-electrolyte interface (SEI) on the surface of the material during oxygen loss on charging to 4.8 V.[5] Though the composition of the amorphous surface layer is undetermined. Recently Kang and Thackeray reported a new surface coating of Li–Ni–PO_4, which leads to reversible capacity of 200 mAh/g at C/1 rate.[13] They speculated that one of the component Li_3PO_4 acts as an excellent lithium ion conductor as well as an efficient protective layer stabilizing the electrode surface, though it is not clear how would Li_3PO_4 stabilizes the electrode surface.

Despite much work on this family of materials, a detailed understanding regarding the stability of the surface of the material is still lacking. In depth investigations are necessary to indentify surface structural changes associated with the cation migrations in the *pristine* layered lithium-excess oxides. In this work, we carried out Synchrotron X-Ray Diffraction (XRD), aberration corrected Scanning Transmission Electron Microscopy (*a*-S/TEM) and Electron Energy Loss Spectroscopy (EELS) combined with electrochemical testing on $Li[Ni_{1/5}Li_{1/3-2x/3}Mn_{2/3-x/3}]O_2$ ($x = 1/5$) compounds to identify how the surface and bulk changed after the first charge/discharge cycle. First principles computation was performed on the model compound $Li[Ni_xLi_{1/3-2x/3}Mn_{2/3-x/3}]O_2$ ($x = 1/4$) to help guide the experimental investigations and better rationalize the highly complicated experimental observations.

Methodologies

Synthesis

A novel coprecipitation technique was used for the synthesis of the materials which was previously described.[10] Transition metal nitrates, $Ni(NO_3)_2 \cdot 6H_2O$(Fisher) and $Mn(NO_3)_2 \cdot 4H_2O$ (Fisher), were titrated into a stoichiometric $LiOH \cdot H_2O$ solution for a duration of two hours. The co-precipitated transition metal hydroxides were then filtered using a vacuum filter and washed three times with deionized water. The collected transition metal hydroxides were dried in an oven at 180 °C for 10 h in air. The dried transition metal precursors were mixed with a stoichiometric amount of $LiOH \cdot H_2O$ corresponding to the amount of M $(OH)_2$ from the coprecipitation step. This mixture was ground for 30 min to ensure adequate mixing and then placed into a furnace at 480 °C for 12 h. The precalcinated powders were prepared as a pellet for high temperature sintering. These samples were then calcinated at 1000 °C for 12 h in air. Samples were brought back to room temperature by furnace cooling.

Electrochemistry

For the electrochemical charge/discharge at different C-rate and cycling experiments, cathodes were prepared by mixing the $Li[Ni_{1/5}Li_{1/5}Mn_{3/5}]O_2$ with 10 wt% Super P carbon (TIMCAL) and 10 wt% poly-vinylidene fluoride (PVDF) in N-mythyl pyrrolidone (NMP) solution. The slurry was cast onto an Al foil using a doctor blade and dried in a vacuum oven at 80 °C. The electrode discs were punched and dried again at 80 °C for 6 h before storing them in an argon filled glove box (H_2O level < 2 ppm). 2016 type coin cells were used to study the electrochemical behavior of the compounds and cycled samples for XRD and TEM. Lithium metal ribbon and 1M $LiPF_6$ in a 1 : 1 ethylene carbonate : dimethyl carbonate (EC : DMC) solution (Novolyte) were used as the counter electrode and electrolyte, respectively. Celgard model C480 separator (Celgard Inc, USA) was used as the separator. The coin-cells were assembled in an argon filled glove box and tested on an Arbin battery cycler in the galvanostatic mode. The tests were conducted between 2.0 and 4.8 V at a constant current rate of C/50 unless otherwise mentioned. Electrochemical impedance spectroscopy (EIS) measurements were carried out using a Solartron 1287 & Solartron 1260 frequency response analyzer system at room temperature with metallic lithium as the counter and reference electrodes in the frequency range of 10 kHz to 10 mHz at an AC voltage of 10 mV. The cell voltage was potentiostatically stepped at 20 mV increments and held. The EIS measurement began at each held voltage when the measured current fell below a current of 10μA corresponding to a C/200 rate.

The samples for XRD and TEM were recovered by disassembling cycled batteries in an argon-filled glovebox. The cathode was washed by Acetonitrile (H_2O < 10 ppm) 3 times. The cathode was allowed to dry in Argon atmosphere overnight. The powder was scraped and mounted in a hermitically sealed capillary for ex-situ X-ray diffraction. For ex-situ TEM sample preparation, the powders were suspended on a copper grid with lacey carbon. The approximate time of sample exposed to air (from a sealed environment to the microscope column) is less than 10 s.

X-ray diffraction

Powder diffractions of all samples were taken using synchrotron X-ray diffraction at the Advanced Photon Source (APS) at Argonne National Laboratory (ANL) on beamline 11-BM (λ = 0.4122 Å). Cycled samples were hermetically sealed in 1.0 mm kapton capillaries to minimize air-exposure. The beamline uses a sagittally focused X-ray beam with a high precision diffractometer circle and perfect Si(111) crystal analyzer detection for high sensitivity and resolution. Instrumental resolution at high Q is better than $\Delta Q/Q \approx 2 \times 10^{-4}$, with a typical 2θ resolution of < 0.01° at 30 keV XRD data analysis was carried out by Rietveld refinement method using FullProf and GSAS/EXPGUI software.[14–16]

a-STEM/EELS

Electron Microscopy work was carried out on a Cs-corrected FEI Titan 80/300 kV TEM/STEM microscope equipped with a Gatan Image Filter Quantum-865. All STEM images and EELS spectra were acquired at 300 kV and with a beam size of ~0.7 Å. EELS spectra shown in this work were acquired from a square area of ~0.5*0.5 nm with an acquisition time of 3 s and a collection angle of 35 mrad. HAADF images are obtained with a convergence angle of 30 mrad and a large inner collection angle of 65 mrad. To minimize possible electron beam irradiation effects, EELS and HAADF figures here are acquired from areas without pre-beam irradiation.

Computation methods

The first principles calculations were performed in the spin-polarized GGA + U approximations to the Density Functional Theory (DFT). Core electron states were represented by the projector augmented-wave method[17] as implemented in the Vienna ab initio simulation package (VASP).[18–20] The Perdew–Burke–Ernzerhof exchange correlation[21] and a plane wave representation for the wavefunction with a cutoff energy of 450 eV were used. The Brillouin zone was sampled with a dense k-points mesh by Gamma packing. The supercell is composed of twelve-formula units of $Li[Ni_{1/4}Li_{1/6}Mn_{7/12}]O_2$. The lattice shows a $R\bar{3}m$ layered structure. The atomic positions and cell parameters are fully relaxed to obtain total energy and optimized cell structure. To obtain the accurate electronic structures, a static self—consistent calculation is run, followed by a non—self—consistent calculation using the calculated charge densities from the first step. The cell volume is fixed with internal relaxation of the ions in the second step calculation. The Hubbard U correction was introduced to describe the effect of localized d electrons

of transition metal ions. Each transition metal ion has a unique effective U value applied in the rotationally invariant LSDA + U approach.[22] The applied effective U value given to Mn ions is 5 eV and to Ni ions is 5.96 eV, consistent with early work on $LiNi_{1/2}Mn_{1/2}O_2$.[23]
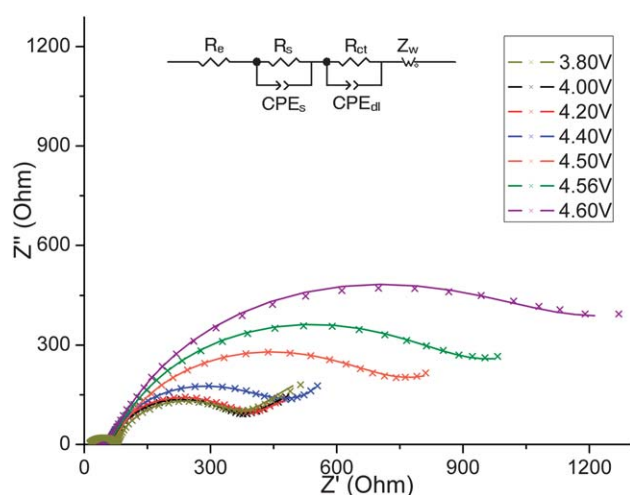
Results

Electrochemical properties

Electrochemical measurements of $Li[Li_{1/5}Ni_{1/5}Mn_{3/5}]O_2$ electrodes were performed in lithium half-cells cycled between 2.0 to 4.8 V. Fig. 1a displays the voltage (V) *versus* capacity (mAh/g) electrochemical curves for $Li[Li_{1/5}Ni_{1/5}Mn_{3/5}]O_2$ in galvanostatic mode at C/50 for the first charge/discharge cycle. During the first charge step, the voltage in the cell increases monotonically until 4.4 V, and reaches a plateau region between 4.4 and 4.6 V. The discharge capacity of first cycle is 255 mAh/g, around 50 mAh/g less than the first cycle charge capacity. Fig. 1b shows the capacity *versus* cycle number of $Li[Ni_{1/5}Li_{1/5}Mn_{3/5}]O_2$ electrodes. The material shows steady reversible cycling reaching capacities exceeding 200 mAh/g at C/50 and C/20 rates. Electrochemical
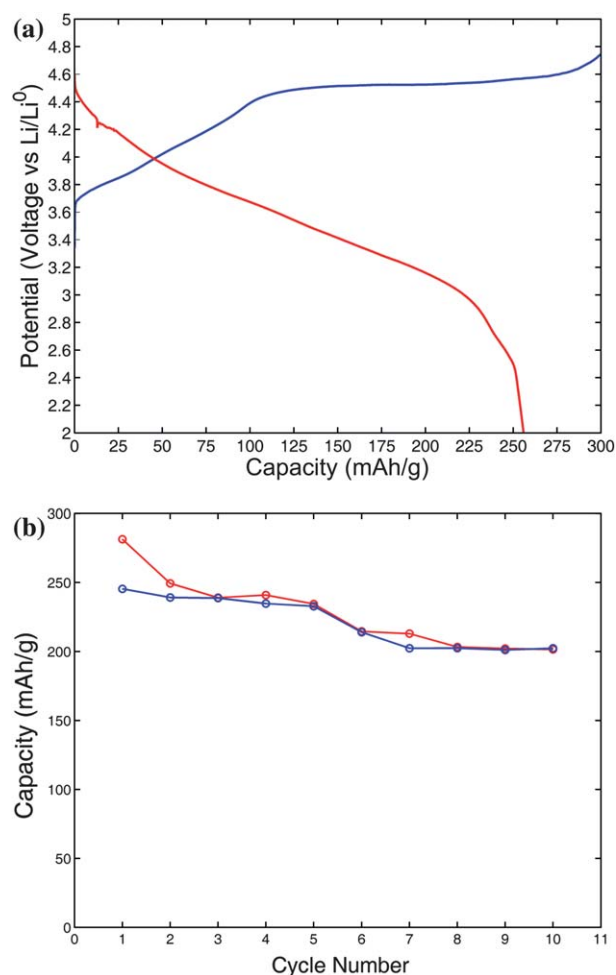
Fig. 1 (a) Electrochemical profile of $Li[Ni_xLi_{1/3-2x/3}Mn_{2/3-x/3}]O_2$ (x = 1/5) with a C/50 rate. A voltage window of 4.8–2.0 V was used. (b) Capacity *versus* electrochemical cycle of $Li[Ni_{1/5}Li_{1/5}Mn_{3/5}]O_2$. The first 5 cycles correspond to a C/50 rate and cycles 6-1 correspond to a C/20 rate.

impedance spectroscopy (EIS) was performed to study the change of impedance in the Li[Li$_{1/5}$Ni$_{1/5}$Mn$_{3/5}$]O$_2$/Li half cell as a function of the state of charge (SOC). Fig. 2 compares the EIS spectra of the cell at 3.8, 4.0, 4.2, 4.4, 4.5 and 4.6 V. The impedance spectra were analyzed using physical processes that could be represented as a combination of resistive/capacitive elements. Due to the nonhomogeneity of the composite electrode system reflected as depressed semicircles in the impedance response, constant phase elements are used in place of capacitors to model the data. The equivalent circuit in the insert of Fig. 2 was used for fitting of the data. The cross points are experimentally measured data and the line is from the equivalent circuit fitting. Table 1 shows the values obtained from the equivalent circuit fitting of the electrolyte resistance, R$_e$, surface resistance, R$_s$ and charge transfer resistance, R$_{ct}$. At low voltages, the figure exhibits two depressed semicircles at the high frequency regimes and a sloped line at low frequencies. The impedance spectra changes shape as the voltage increases. The size of the second lower frequency semicircle increases in diameter and the sloped line disappears as the voltage increases from 4.40 V to 4.60 V. The distinct regions on the figure represent separate time constants in the delithiation process. The first semicircle in the high frequency region is potential independent and represents the lithium ion diffusion across the electrode/electrolyte (solid/liquid) interface. The intercept of the first semicircle at the highest frequency with the real axis (Z$_{re}$) corresponds to the ohmic resistance originating from the electrolyte (R$_e$). The second semicircle in the middle frequency region is related to the charge transfer region between the surface film and the Li[Li$_{1/5}$Ni$_{1/5}$Mn$_{3/5}$]O$_2$ particle interface. The diameter of this second semicircle represents the charge transfer resistance (R$_{ct}$). At lower voltages (up to 4.4 V) and lower frequencies, a narrow Warburg region is followed by a sloped line. This region is attributed to solid-state diffusion of Li ions into the bulk cathode material.[24] Before the plateau region at 3.80, 4.00, 4.20 and 4.40 V, the surface resistance R$_s$ reduces slightly, while the solid
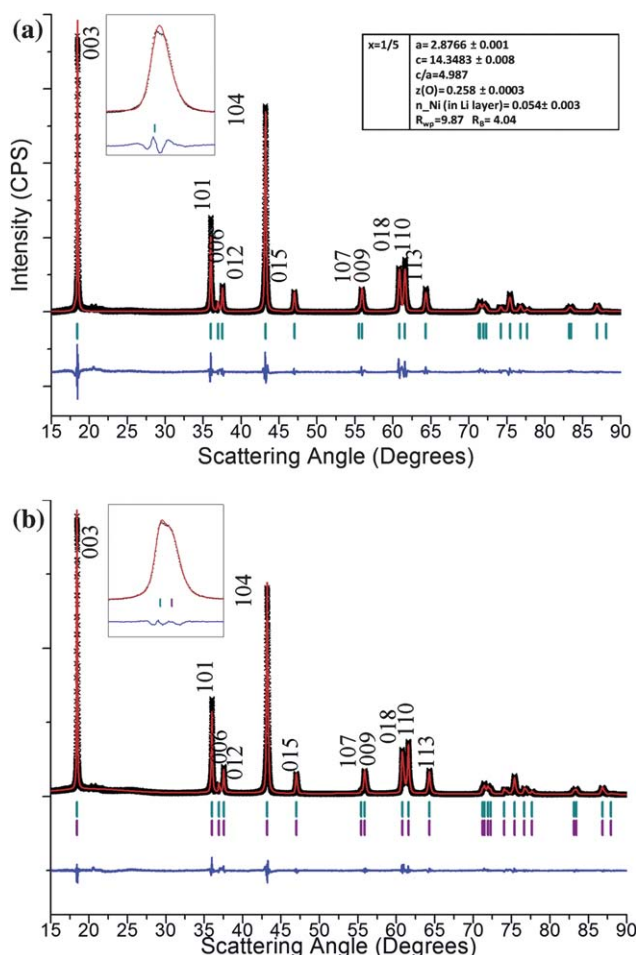
Table 1 Fitting parameters for the equivalent circuit model represented in Fig. 2 applied to the electrochemical impedance (EIS) curves recorded between 3.80 V and 4.60 V

Voltage	Re	Rs	Rct
3.80 V	11.3	63	245
4.00 V	11.4	49.9	284.2
4.20 V	11.4	40.6	254.4
4.40 V	11.7	38.4	319.4
4.50 V	13.2	44.1	552.7
4.56 V	13.0	39.2	713.3
4.60 V	12.9	36.7	925.5

diffusion represented by the linear Warburg region and the charge transfer resistance remain relatively constant. Once the voltages reach the plateau region between 4.50 and 4.60 V, the surface resistances remain relatively constant, while the major changes in the spectra is dominated by a significant increase in the charge transfer resistance (R$_{ct}$). This trend is in contrast with other conventional layered transition metal oxide cathode materials (e.g. LiCoO$_2$) where R$_{ct}$ was observed to decrease with the states of charge.[24,25]

XRD

X-Ray diffraction pattern of pristine Li[Li$_{1/5}$Ni$_{1/5}$Mn$_{3/5}$]O$_2$ shows the pristine phase is a typical well layered phase with <3% Li/Ni mixing (see supporting information Fig. S1†). X-Ray diffraction pattern of the material following 10 electrochemical cycles are shown in Fig. 3 and refined using a single $R\bar{3}m$ phase (Fig. 3a) as listed in the inset table. The superlattice peaks between 20–30° observed in pristine materials disappeared in the cycled materials. Based on the capacities observed, the cycled material has 0.8 Li remaining in the structure. Compared to the pristine materials, a significant c lattice expansion is observed accompanied by an increased amount of Li/Ni interlayer mixing. The Rietveld refinement using a single layered phase provides reasonably good fitting based on the R$_{wp}$ and R$_b$ fitting factors; however, large mismatch of the (003) peak can be observed clearly as shown in the inset in Fig. 3a. To correct this mismatch, a two-phase refinement including a second $R\bar{3}m$ phase was performed. The fitting pattern is shown in Fig. 3b and the refinement results are listed in Table 2. Both of the layered phases show an expanded lattice, however one phase shows little Li/Ni interlayer mixing and the other layered phase shows increased Li/Ni mixing compared to the pristine material. The inset in Fig. 3b shows significant improvement in fitting of the (003) peak based on two phases. Rietveld refinement included tetrahedral Li ions in one of the two layered phase was also performed and the results are listed in Table 3. R$_{wp}$ and R$_B$ fitting factors can be further reduced when ~13% tetrahedral Li ions are included. More details on the formation of tetrahedral Li will be discussed later.

Fig. 2 Experimental observations (marked by X) of electrochemical impedance spectroscopy (EIS) of Li[Ni$_{1/5}$Li$_{1/5}$Mn$_{3/5}$]O$_2$ during the first electrochemical charging cycle at different states of charge (SOC) The equivalent circuit model in the inset was used to fit the experimental model and plotted as a line at different SOC.

Fig. 3 High resolution synchrotron X-ray diffraction pattern of discharged Li[Ni$_{1/5}$Li$_{1/5}$Mn$_{3/5}$]O$_2$ following 10 electrochemical cycles. Rietveld Refinement of (a) one $R\bar{3}m$ phase and (b) two $R\bar{3}m$ phases. The black crosses represent the observed pattern, the red line corresponds to the calculated diffraction pattern and the blue is the difference pattern. The teal lines correspond to peak positions from the $R\bar{3}m$ space group. In this and subsequent figures, the 2θ values are converted to those corresponding to a Cu-Kα wavelength ($\lambda = 1.54$ Å).

STEM

Fig. 4 and 5 depict electron microscopy data from the pristine sample and cycled sample (at the discharge state after 10 cycles between 2 to 4.8 V). The particles show a high degree of crystallinity and well faceted surfaces. Multiple grains were selected for study and the results are consistent, therefore only representative data are shown here. Images acquired by an HAADF detector with a small convergence angle and a relative large inner collection angle are also called "Z-contrast" images, where the contrast is proportional to $Z^{1.7}$.[26,27] In atomic resolution Z-contrast images, the contrast of the atomic columns thus can be used to differentiate different elements and provide atomic-structural information.

Fig. 4a is a typical Z-contrast image recorded along the [100] zone axis and Fig. 4b shows a high magnification image from a selected area in Fig. 4a. The arrays of atomic columns are clearly revealed. The atomic columns in the horizontal direction are separated by a distance of 4.3 Å, corresponding to the (100)

Table 2 Two phase Rietveld refinement results for discharged Li[Ni$_{1/5}$Li$_{1/5}$Mn$_{3/5}$]O$_2$ following 10 electrochemical cycles using two $R\bar{3}m$ phases[a]

a$_{hex}$: 2.8758 Å		c$_{hex}$: 14.3750			
				c/a: 4.999	$R\bar{3}m$
Atom	Site	Wyckoff positions			Occupancy
Ni1	3a	0	0	0	0.104
Ni2	3b	0	0	0.5	0.096
Mn1	3a	0	0	0	0.600
Li2	3b	0	0	0.5	0.696
Li1	3a	0	0	0	0.104
O	6c	0	0	0.258(3)	2

[a] Conventional Rietveld reliability factors: R$_{wp}$: 7.33 R$_b$: 4.04.

a$_{hex}$: 2.8763 Å		c$_{hex}$: 14.3225			
				c/a: 4.979	$R\bar{3}m$
Atom	Site	Wyckoff positions			Occupancy
Ni1	3a	0	0	0	0.178
Ni2	3b	0	0	0.5	0.022
Mn1	3a	0	0	0	0.600
Li2	3b	0	0	0.5	0.771
Li1	3a	0	0	0	0.029
	6c	0	0	0.258(3)	2

projection of √3a superlattice in $R\bar{3}m$ layered structure; and 4.8 Å in the vertical direction, corresponding to 1/3 of typical c lattice in $R\bar{3}m$ layered structure. The zoomed-in image in Fig. 4b clearly shows a pattern of two brighter columns followed by a darker column; such pattern is a direct result of the cation ordering in the TM plane: Two TM-rich columns (higher Z) and one Li-rich column (lower Z). An atomistic model is placed next to the HAADF image for clarity. The well layered properties in the bulk of the pristine material extend to the surface. Moreover, the stacking sequence of the ordered TM layers along the (001) c-direction is random. Our observations are consistent with previous report on uncoated pristine LiLi$_{1/5}$Ni$_{1/5}$Mn$_{3/5}$O$_2$ material by Lei et.al.

Fig. 5a shows traditional bright field images of the surface and bulk of the material following 10 electrochemical cycles recorded along the [100] zone axis. A 2–5 nm amorphous layer was observed on the surface of the material, which might be related to the side reaction of electrolyte at high voltage (>4.5 V). Detailed analysis of this layer will be discussed in a separated paper. The HAADF image in Fig. 5b shows that the bulk of the grains still maintain the well layered structure as in seen in Fig. 4. The surface structure of the cycled grains, however, is obviously changed based on the contrast change of the atomic columns. Along the (001) direction, the dark columns of bulk (Li atomic columns) become much brighter on the surface. In fact, their contrast is almost comparable to their neighboring TM columns. This suggests that a significant amount of transition metal ions migrate into the Li sites resulting in a loss of the layered characteristics at the surface of the materials.
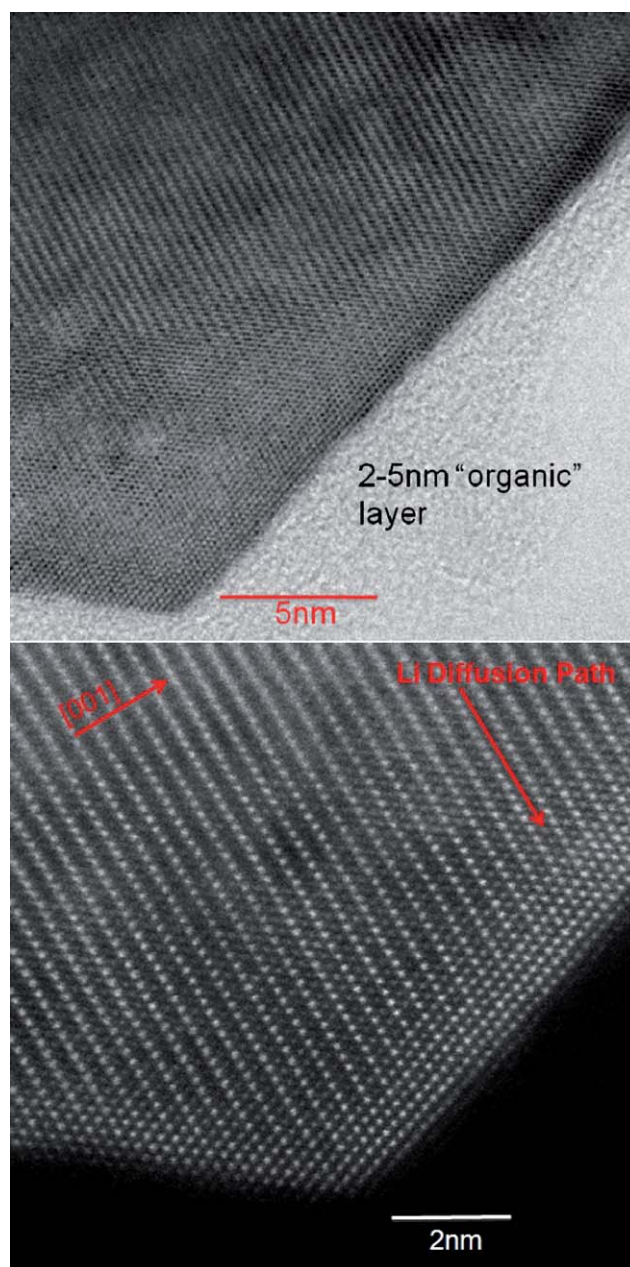
EELS

Fig. 6a compares the EELS spectra of the oxygen K-edge and the manganese L$_3$ and L$_2$ edges from the surface and bulk of the
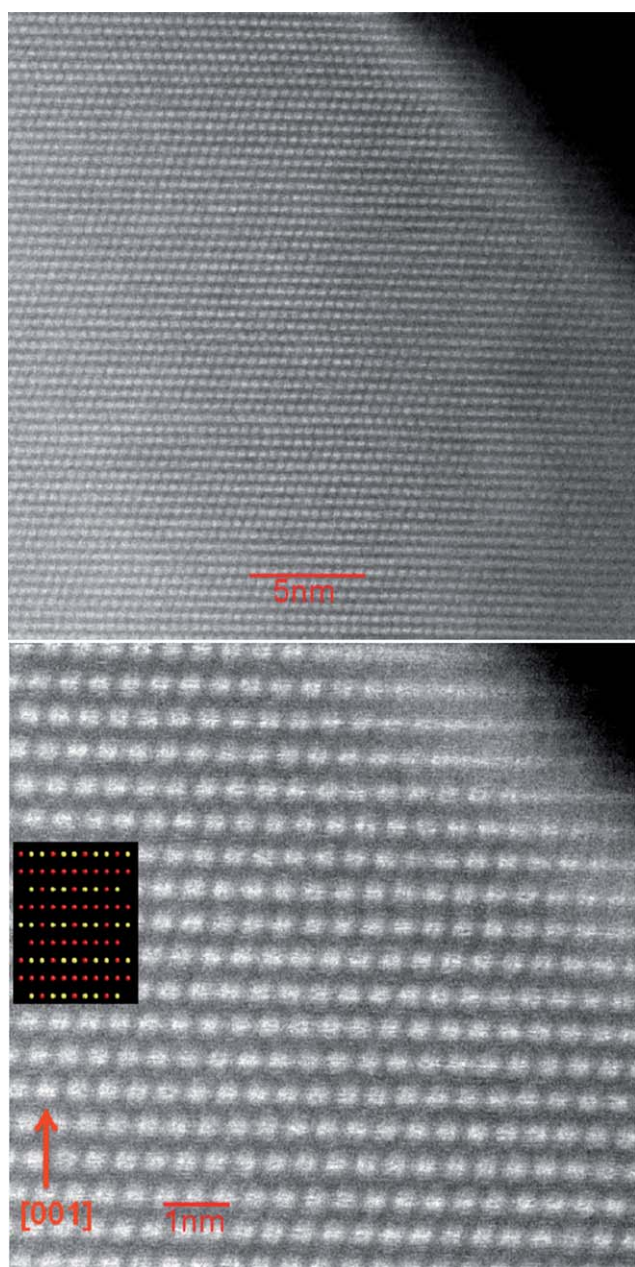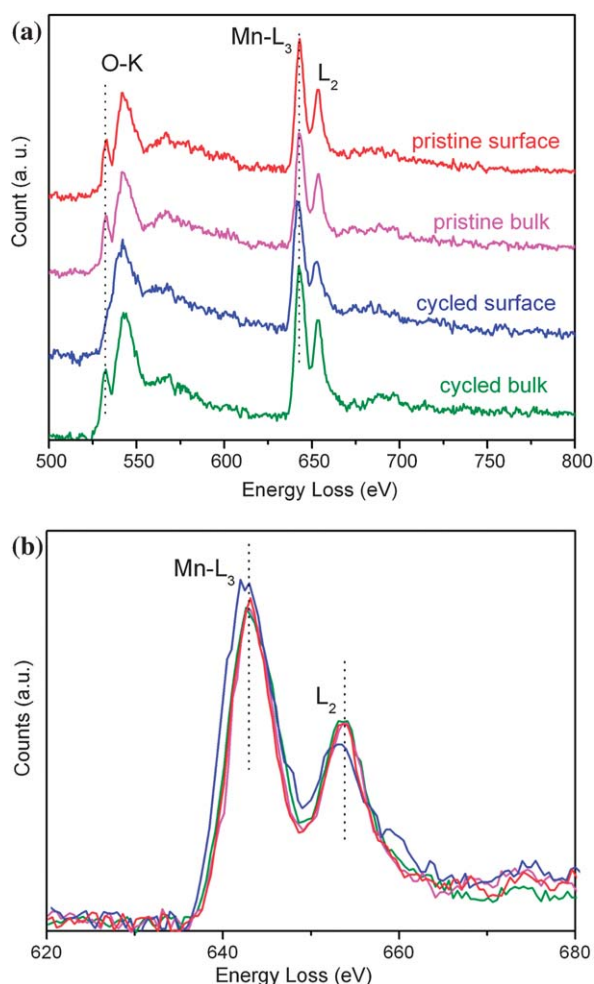
Fig. 4 High resolution S/TEM images of the bulk and surface of pristine Li[Ni$_{1/5}$Li$_{1/5}$Mn$_{3/5}$]O$_2$ at low magnification (a) and high magnification (b) taken along [100]. The insert in (b) is a schematic representation of the Li ions (red) and transition metal ions (yellow) showing the cation ordering and stacking along the chex axis.

Fig. 5 High resolution S/TEM image (a) and corresponding HAADF image (b) of the bulk and surface regions of electrochemically cycled Li [Ni$_{1/5}$Li$_{1/5}$Mn$_{3/5}$]O$_2$ taken along the [110] zone axis.

pristine and cycled samples respectively. The fine structure and energy position of O–K and Mn-L edges imprints the electronic structure of the sample and thus can be used to study the structural evolution on the cycled surface. The energy position and fine structures of Mn-L edges are almost identical on the spectra from the pristine surface and bulk, and the cycled bulk. However, those from the cycled surface area slightly shift to a lower energy loss, which indicates a decreased oxidation state of Mn. This is also proved by its relatively higher L$_3$/L$_2$ ratio, which is a well-known indicator of oxidation state variations in transition metals.[28,29] Fine-structure modifications of O–K edges

are noticeable on the spectrum from the cycled surface compared to the other spectra. The first peak, at energy loss of ~532 eV almost vanished on the spectrum from the cycled surface. This O-prepeak can be attributed to the transition of 1 s core state to the unoccupied O-$2p$ states hybridized with TM-$3d$ states. The decreased intensity of this peak on the cycled surface likely indicates the modification of unoccupied states of TM-$3d$ and bonding lengths of TM-TM. These electronic structure changes correlate well with the atomic structure modification revealed by Z-contrast imaging. EELS quantification shows that O/Mn ratio variation among the cycled surface and bulk is less than 5%, which imply no significant oxygen losses in the cycled sample. In contrast, obvious Li loss (more than 50%) was found on the

Fig. 7 Comparison of Li–K edges from the surface and bulk in the cycled material. Obvious Li signal drop was observed on the spectrum from the surface area compared to that from bulk, although Li–K edge overlaps TM-M edges. Dotted lines mark the main peak position of Li–K and TM-M edges.
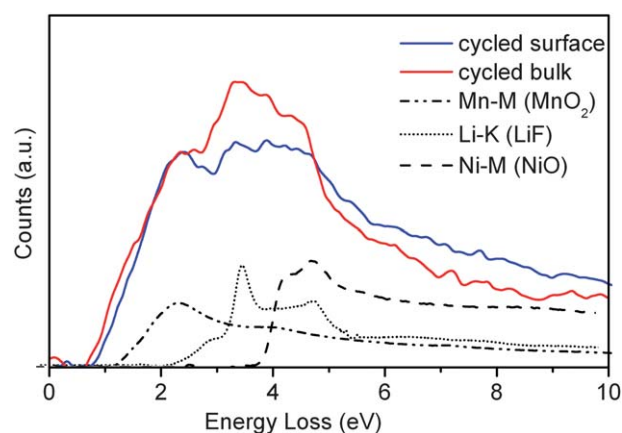

Fig. 6 Representative EELS spectra of the (a) O K-edge and (a & b) Mn L-edge from the surface and bulk of the pristine and electrochemically cycled $Li[Ni_{1/5}Li_{1/5}Mn_{3/5}]O_2$ material.

cycled surface, see Fig. 7. This is consistent with the fact that significant TM atoms occupy Li site on the cycled surface, which is revealed by Z-contrast imaging (Fig.5).

First-principles calculations

The compound $Li[Ni_{1/4}Li_{1/6}Mn_{7/12}]O_2$ is modelled as a solid solution of Li_2MnO_3 and $LiNi_{0.5}Mn_{0.5}O_2$. For the convenience to interpret computation results, the formula of this compound will also be referred as $Li_{14/12}Ni_{1/4}Mn_{7/12}O_2$. There are four layers in each suprecell, two oxygen layers, one transition metal (TM) layer and one Li layer. Each layer is composed of twelve ions, forming a $2\sqrt{3}a_{hex} \times 2\sqrt{3}a_{hex}$ in-plane supercell. Oxygen ions are close-packed and stacked in ABC (O3) stacking, serving as the frame, while TM slab and Li slab stack alternatively. Several models of fully-lithiated $Li_{n/12}Ni_{3/12}Mn_{7/12}O_2$ (n = 14) are created and the calculated total energies are compared (results are shown in supporting information Fig. S2–S4†). In the model with the lowest energy, Li layer supercell is composed of 12 Li ions (Fig. 8b) and the in-plane cation ordering of the TM layer is shown in Fig. 8a. There are two "excess" Li ions located in the TM layer, one Li ion is surrounded by 6 Mn ions and the

Fig. 8 (a)&(b) The cation in-plane ordering of different models of Li $[Ni_{1/4}Li_{1/6}Mn_{7/12}]O_2$ (Red: Li; Green: Mn; Blue: Ni) (c) Calculated voltage and formation enthalpy of $Li_{x/14}Ni_{1/4}Mn_{7/12}O_2$ (8 < x < 14) versus lithium concentration.

other Li ion is surrounded by 5 Mn ions plus 1 Ni ion. The Ni ions are arranged in the "broken zigzag" shape. In this model the cation arrangements are most consistent with experimental observations including NMR[2], electron diffraction[4] and X-ray diffraction and is used as the basis to investigate the lithium

de-intercalation mechanism of the materials. Although the models we propose here are all solid-solutions of Li_2MnO_3 and $LiNi_{0.5}Mn_{0.5}O_2$, phase separations may happen. The mixing energy calculated by following equation is around +40 meV per formula. Note that in the synthesis of this series of materials, 900–1000 °C heating temperature is used, that very likely overcomes a small positive mixing energies.

$$\Delta E_{mixing} = E_{Li[Ni_{1/4}Li_{1/6}Mn_{7/12}]O_2} - 0.5*(E_{Li_2MnO_3} + E_{LiNi_{0.5}Mn_{0.5}O_2})$$

The formation enthalpy of $Li_{n/12}Ni_{1/4}Mn_{7/12}O_2$ (8 < n < 14) *versus* lithium concentration is calculated with two reference states set as n = 8 and n = 14 (Fig. 8c). When n = 8, all Ni ions are oxidized to the highest valence state. Further removal of Li ions beyond this critical lithium concentration will result in the additional capacities related to non-redox centers. The calculated voltages (shown in red line in the inset of Fig. 8c) range from 3.86V to 4.48V, match well with the experimental measurements of the 1st cycle charging voltage (shown in black line in the inset of Fig. 8c). At each concentration, various Li-vacancy configurations are calculated and those with the lowest energies are depicted by red crosses in Fig. 8c. These configurations usually involve tetrahedral Li ions (Li_{tet}) formed in the Li layer. Structures of Li_{oct}-vacancy configurations are also investigated and the most stable configurations are depicted by the green dots. Below certain lithium concentrations (n < 11), however, these configurations usually have higher energies. The blues stars in Fig. 8c depict the structures based on a defect spinel model as illustrated in Fig. 9. In the defect-spinel model, the Li layer supercell is composed of 11 Li ions with 1 Ni ion, and the TM layer in-plane cation ordering is shown in Fig. 9a. When n = 14, the TM ions in the TM layer are arranged following the Mn lattice in [111] plane of spinel $LiMn_2O_4$ illustrated in Fig. 9b. Therefore, when n = 8, the formula of the compound $Li_{2/3}Ni_{1/4}Mn_{7/12}O_2$ can be re-written as $Li[Li_{1/3}Ni_{1/2}Mn_{7/6}]O_4$, forming a Li-excess defect-spinel phase where part of the *16d* octahedral sites are occupied by Li ions (Fig. 9c). In a perfect spinel phase, only transition metal ions reside on *16d* sites. At fully lithiated state (n = 14), the formation enthalpy of this defect-spinel phase is +105 meV and at x = 8 the formation enthalpy of this phase is −101 meV with respect to the corresponding layered form.

Calculations of electronic structures are performed on $Li_{n/12}Ni_{1/4}Mn_{7/12}O_2$ at (0 < n < 14). For n < 8, structures are
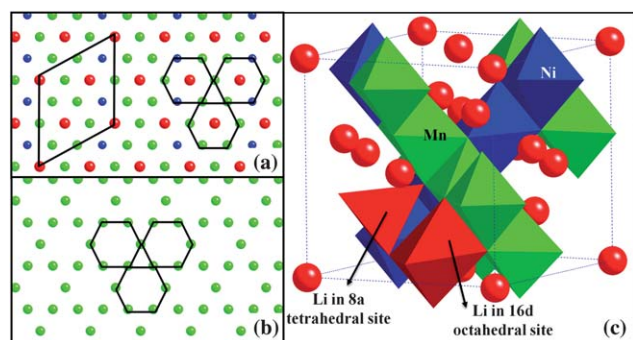

Fig. 9 The defect-spinel model of $Li[Ni_{1/4}Li_{1/6}Mn_{7/12}]O_2$ and $Li[Li_{1/3}Ni_{1/2}Mn_{7/6}]O_4$.
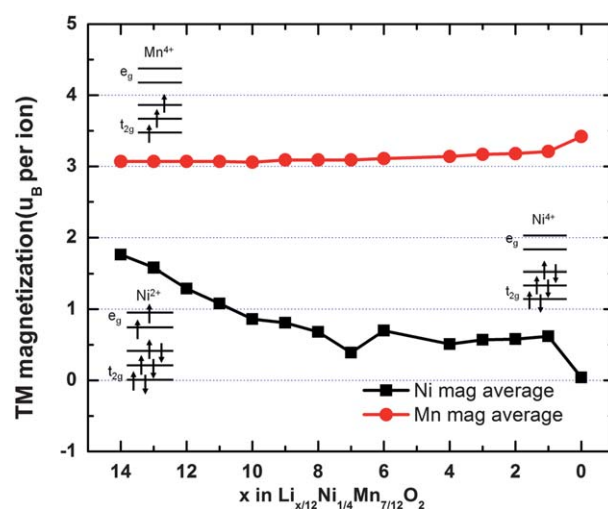
Fig. 10 Calculated magnetization of Ni and Mn ions *versus* lithium concentration.

modeled without introduction of oxygen vacancies. The valences of TM ions are estimated from the calculated TM magnetizations. The electron configurations of TM ions within octahedral ligand fields are shown in Fig. 10 insets. In Fig. 10, the average of Ni and Mn magnetizations are plotted *versus* lithium concentration. For Mn ions, the average magnetization retained is $3.1\mu_B$ per ion when n > 8, consistent with a high spin Mn^{4+}. It increases slightly to $3.4 \mu_B$ per ion when n < 8, mainly due to the significant charge redistribution around oxygen ions. Careful inspection of the projected density of the state (see supporting information Fig. S5†) of Mn ions confirm that the valence state of Mn is unchanged as 4+. For Ni ions, the average magnetizations reduces from $1.7 \mu_B$ per ion to $0.4 \mu_B$ per ion when n > 8. This is expected as all high spin Ni^{2+} ions are oxidized to low spin Ni^{4+}, which has been seen experimentally.[30] When n < 8, the average Ni magnetizations fluctuates around $0.5 \mu_B$. It suggests that the valence of Ni ions remains unchanged. The valence of oxygen ions can also be investigated qualitatively from the change of spin distribution over oxygen layer. Three different states of charge are shown in Fig. 11. For clarity, in Fig. 11a part of the oxygen layers of $Li_{n/12}Ni_{1/4}Mn_{7/12}O_2$ supercell is presented by the pink balls together with the adjacent TM slab. The corresponding spin density of this region at n = 14, 8, and 0, are presented respectively in Fig. 11b, c, and d. Though the plane cut through oxygen layer, positive spin density of Ni and Mn ions can still be observed partially. At full lithium concentration (n = 14), well bonded oxygen *2p* electrons can be clearly observed in Fig. 11b. However, the shape of oxygen *2p* electron clouds begins to distort at lower lithium concentration (n = 8, Fig. 11c), suggesting a potential change of oxygen valence. At n = 0 (Fig. 11d), the spin distribution around oxygen ions change significantly. The spin densities of Mn ions also increase slightly, possibly due to weakening of Mn–O bonding, which is consistent with the change of Mn magnetization as described above. Note that no oxygen vacancies are allowed in current models. The above results indicate that during the charging stage, the extra electrons that cannot be provided by the Ni redox couples are coming from oxygen ions.
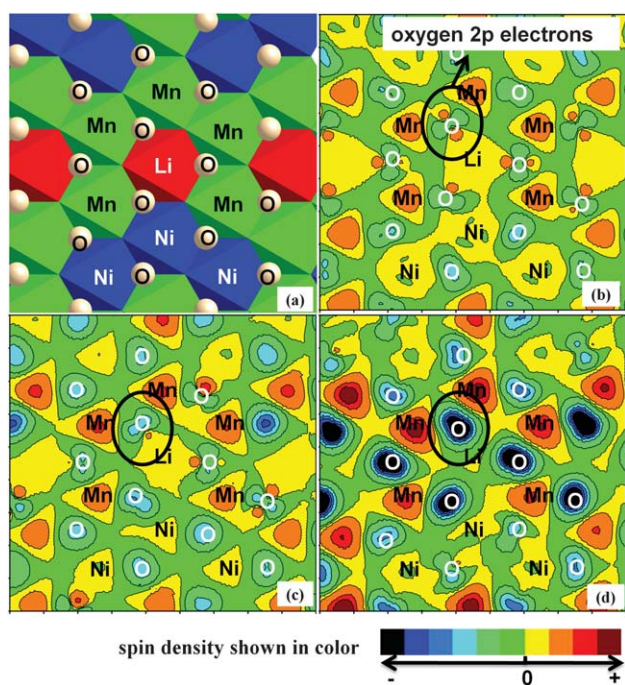
Fig. 11 (a) Sketch of partial oxygen layer in $Li_{x/14}Ni_{1/4}Mn_{7/12}O_2$ (Pink balls: oxygen ions; Colored polyhedrons: adjacent TM slab) and its calculated spin density at (b) x = 14 (c) x = 8 (d) x = 0.

General discussion

The choice of composition for first principles computation is primarily limited by the size of supercell that is reasonable with modern computation resources. So far we have presented all experimental characterization on $Li[Ni_{1/5}Li_{1/5}Mn_{3/5}]O_2$, previous reports and our study on other compositions have proven that the lithium excess layered oxide, $Li[Ni_xLi_{1/3-2x/3}Mn_{2/3-x/3}]O_2$ (0 < x < 1/2) series show similar behavior before, during and following electrochemical cycling.[5,10,31] Therefore the results from both computations and experimental characterizations could be combined to understand the structural and electrochemical properties of this material series from various aspects. The combined results allow us to present an alternative Li de-intercalation mechanism in the Li-excess layered oxides.

There are two distinct regions in the delithiation process. The initial charging region is before the plateau region when the voltage is less than 4.45 V or the amount of Li is greater than 0.8 per formula. The second step is when the voltage is in the plateau region greater than 4.50 V and the concentration of Li^+ ions is less than 0.8 per formula. For the convenience of general discussion, $Li_\delta Ni_{1/5}Mn_{3/5}O_2$ is taken as the example and discussed in following sections.

Initial stage of lithium deintercalation (pre-plateau up to 4.45 V; 0.8 < δ < 1.2)

First principles calculations suggest that a solid solution behavior exists in this region of the delithiation process consistent with previous experimental work.[10] The Li is continuously extracted from the material, which is depicted by the electrochemical curve as a sloping region from the open circuit voltage

to 4.45 V. This region provides 120 mAh/g capacity (0.4 Li per formula unit) and the charge compensation originates from the Ni ions which is consistent with previous X-ray absorption spectroscopy results showing that the Ni^{2+} ions are oxidized to Ni^{4+}.[30] Both the Mn^{4+} and O^{2-} valences are not changed during this region. The computation results predict that lithium will migrate into tetrahedral sites. This process is illustrated in Fig. 12. Initially the Li^+ ions are removed from the Li layer first seen in Fig. 12a. The energy of removing one Li per cell from Li layer is more than 300 meV lower than that from TM layer. The Li ion in the transition metal layer (Li_{TM}) is edge-sharing with three octahedral Li ions (Li_{oct}) in the adjacent Li layer. When these edge-sharing Li_{oct} ions are extracted, a Li^+ ion will migrate from the octahedral site into the tetrahedral site, as shown in Fig. 12b, face-sharing with Li in the TM layer. During this process, the Li in the TM layer will migrate to the shared tetrahedral site in the opposite site forming a Li–Li dumbbell (Fig. 12c) and the total energy of the structure is further reduced. On the other hand, TM ions in the structure may be able to diffuse following similar ways as Li diffusion. Preliminary calculations give the hints that under certain circumstances, Ni^{2+} ($t_{2g}^6 e_g^2$) may migrate from one octahedral site to another adjacent octahedral site through an empty tetrahedral site, with relatively low energy barriers at the beginning of the charge state. Ni ions therefore may diffuse out of the TM layer, diminishing the ordering contrast in the TM layer, and diffuse into the Li layer, increasing the Li/Ni interlayer mixing.

Second stage of lithium deintercalation (plateau up to 4.8V; 0.2 < δ < 0.8)

In the electrochemical voltage profile, a plateau region exists between 4.4V and 4.6V indicating a two-phase reaction. As suggested by first principles calculations, during this region, the remaining Li^+ ions in the octahedral sites are extracted from the Li layer, while the tetrahedral Li–Li dumbbells are very stable and need voltages exceeding 5.0V to be removed. Therefore these Li–Li dumbbells may never be removed during the first cycling up to 4.8V, blocking the empty sites in the TM layer, therefore may partially cause the irreversible capacity during the first cycle. EELS spectra of Li edge (Fig. 7) indicates that the surface has only about half of the Li concentration as the bulk even at the fully discharged state. The tetrahedral Li that remained in the structure combined with the TM ions migrating into the Li layer
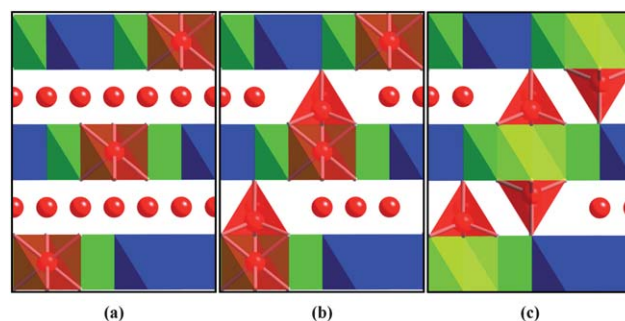
Fig. 12 Sketch of Li–Li dumbbell formation (Red:Li; Green:Mn; Blue: Ni; Yellow: Vacancy).

can facilitate the formation of the proposed spinel-like phase which has an extremely low energy at low lithium concentration regions (high voltage region). Such a second phase may be generated near the surface of the material. The electrochemical impedance data (Fig. 2) shows that the resistance at the interface between the surface layer and the pristine particles dramatically increases especially at high voltages. Such resistance increase may partly be due to the generation of the two phase boundary between the bulk materials and the surface phase. As certain amount of TM ions are now in the Li layers near the surface, as shown by *a*-STEM *Z*-contrast images (Fig. 4 and 5) as well as Rietveld refinement of XRD (Fig. 3), the original Li diffusion planes are populated with high density of TM ions, and the general Li mobility of the material at high voltage (low lithium concentration) is negatively affected. With this specific surface phase structural change, the materials therefore exhibit inferior rate capabilities. Our first principles data, as well as the synchrotron XRD data suggest the formation of tetrahedral Li; however X-ray diffraction is insensitive to Li ions; therefore, the absolute amount of Li present in the tetrahedral layer is still uncertain. Further evidence using neutron diffraction is necessary and will be discussed in a future publication.

The charge compensation mechanism may originate from the oxygen ions as previously explored with the activation of the Li_2MnO_3 region.[1,7] Mn–O bonding is weakening due to the change of the oxygen charge densities, resulting in Mn–O distortions. Typically Mn^{4+} has the t_{2g}^3 electron configuration and MnO_6 octahedrons are highly stable. Such distortion will lead to significant change in the bonding characteristics of Mn–O. EELS observations clearly show that the valence of Mn ions near the surface (about 2–5 nm thick) has been reduced from 4+ and oxygen pre-peak diminished. More careful study on the impact of Mn–O distortions and the possibility of oxygen vacancy formations will be helpful.

Based on the combined experimental and computational results presented, we can conclude that permanent changes occur at the surface of the Li excess layered materials during the initial charging cycle. A new defect-spinel solid phase is formed on the surface of the electrode materials after high-voltage cycling. An atomistic model for such a spinel-like phase is proposed for the first time. We believe that such a surface phase transformation may be part of the sources contributing to the first cycle irreversible capacity and the main reason for the intrinsically poor rate capability of these materials. The surface phase developed in this series of materials following electrochemical cycling is 2–5 nm thick on the surface making it difficult to identify. Characterization of the surface is equally difficult because the oxygen framework remains the same but changes in the transition metal layers and lithium layers appear. The results from this work required the use of sophisticated techniques such as atomic resolution STEM and EELS with high spatial resolution. The atomic contrast STEM images can be used to identify changes in the stacking and ordering within the material while the EELS analysis complements the STEM results with quantifiable changes. The combination of the two techniques provides strong evidence for the growth of a surface layer on the lithium excess series of materials. Our research findings provide significantly new insights to reasons why the surface coatings of these materials improve the electrochemical properties such as rate capabilities and irreversible capacity losses. The study of the role of surface coatings is under way and the present results reinforce the view that this is an important area for expanded research.

Conclusion

The series of Li-excess layered oxide compounds $Li[Ni_xLi_{1/3-2x/3}Mn_{2/3-x/3}]O_2$ ($0 < x < 1/2$) are investigated in a joint study combining both computational and experimental methods. From first principles calculation, a new lithium de-intercalation mechanism is proposed where stable tetrahedral lithium ions are formed during the early charging stage and may not be able to be extracted before 5 V. The Rietveld refinement results from XRD of pristine and cycled samples further confirm that the tetrahedral lithium ions are involved in the cycled samples accompanied by an increase in Li–Ni interlayer mixing. The *Z*-contrast high-resolution TEM also provide the evidence of surface transition metal ions migrating into the lithium layer, which may affect the transition metal–oxygen bonding characteristics as indicated in the EELS results. Such surface structural change may lead to a phase transformation from layered structure to defect-spinel structure at the surface of the materials. The large irreversible capacity after cycling and the low rate capability of the materials are therefore partially attributed to this surface phase transformation.

Acknowledgements

References

1 Z. Lu, D. D. MacNeil and J. R. Dahn, *Electrochem. Solid-State Lett.*, 2001, **4**, A191–A194.
2 C. P. Grey, W. S. Yoon, J. Reed and G. Ceder, *Electrochem. Solid-State Lett.*, 2004, **7**, A290–A293.
3 M. M. Thackeray, S.-H. Kang, C. S. Johnson, J. T. Vaughey, R. Benedek and S. A. Hackney, *J. Mater. Chem.*, 2007, **17**, 3112–3125.
4 Y. S. Meng, G. Ceder, C. P. Grey, W. S. Yoon, M. Jiang, J. Breger and Y. Shao-Horn, *Chem. Mater.*, 2005, **17**, 2386–2394.
5 M. Jiang, B. Key, Y. S. Meng and C. P. Grey, *Chem. Mater.*, 2009, **21**, 2733–2745.
6 C. H. Lei, J. Bareno, J. G. Wen, I. Petrov, S. H. Kang and D. P. Abraham, *J. Power Sources*, 2008, **178**, 422–433.

7   A. R. Armstrong, M. Holzapfel, P. Novak, C. S. Johnson, S. H. Kang, M. M. Thackeray and P. G. Bruce, *J. Am. Chem. Soc.*, 2006, **128**, 8694–8698.
8   Z. Lu and J. R. Dahn, *J. Electrochem. Soc.*, 2002, **149**, A815–A822.
9   A. D. Robertson and P. G. Bruce, *Electrochem. Solid-State Lett.*, 2004, **7**, A294–A298.
10 C. R. Fell, K. J. Carroll, M. Chi and Y. S. Meng, *J. Electrochem. Soc.*, 2010, **157**, A1202–A1211.
11 J. M. Zheng, Z. R. Zhang, X. B. Wu, Z. X. Dong, Z. Zhu and Y. Yang, *J. Electrochem. Soc.*, 2008, **155**, A775–A782.
12 Y. Wu and A. Manthiram, *Solid State Ionics*, 2009, **180**, 50–56.
13 S. H. Kang and M. M. Thackeray, *Electrochem. Commun.*, 2009, **11**, 748–751.
14 J. Rodríguez-Carvajal, in *Satellite Meeting on Powder Diffraction of the XV Congress of the IUCr*, Toulouse, France, 1990, p. 127.
15 B. Toby, *J. Appl. Crystallogr.*, 2001, **34**, 210–213.
16 A. C. Larson and R. B. V. Dreele, Los Alamos National Laboratory Report LAUR, 2000, 86.
17 G. Kresse and D. Joubert, *Phys. Rev. B: Condens. Matter Mater. Phys.*, 1999, **59**, 1758–1775.
18 G. Kresse and J. Hafner, *Phys. Rev. B: Condens. Matter*, 1994, **49**, 14251–14269.
19 G. Kresse and J. Furthmuller, *Comput. Mater. Sci.*, 1996, **6**, 15–50.
20 G. Kresse and J. Furthmuller, *Phys. Rev. B: Condens. Matter*, 1996, **54**, 11169–11186.
21 J. P. Perdew, K. Burke and Y. Wang, *Phys. Rev. B: Condens. Matter*, 1996, **54**, 16533–16539.
22 A. I. Liechtenstein, V. I. Anisimov and J. Zaanen, *Phys. Rev. B: Condens. Matter*, 1995, **52**, R5467–R5470.
23 Y. Hinuma, Y. S. Meng, K. S. Kang and G. Ceder, *Chem. Mater.*, 2007, **19**, 1790–1800.
24 M. D. Levi, G. Salitra, B. Markovsky, H. Teller, D. Aurbach, U. Heider and L. Heider, *J. Electrochem. Soc.*, 1999, **146**, 1279–1289.
25 D. Aurbach, M. D. Levi, E. Levi, H. Teller, B. Markovsky, G. Salitra, U. Heider and L. Heider, *J. Electrochem. Soc.*, 1998, **145**, 3024–3034.
26 S. J. Pennycook, *Ultramicroscopy*, 1989, **30**, 58–69.
27 E. M. James and N. D. Browning, *Ultramicroscopy*, 1999, **78**, 125–139.
28 R. F. Egerton, *Electron Energy-Loss Spectrosopy in the Electron Microscope*, Plenum Press, New York, 1996.
29 Z. L. Wang, J. S. Yin and Y. D. Jiang, *Micron*, 2000, **31**, 571–580.
30 W. S. Yoon, Y. Paik, X. Q. Yang, M. Balasubramanian, J. McBreen and C. P. Grey, *Electrochem. Solid-State Lett.*, 2002, **5**, A263–A266.
31 Z. Lu, L. Y. Beaulieu, R. A. Donaberger, C. L. Thomas and J. R. Dahn, *J. Electrochem. Soc.*, 2002, **149**, A778–A791.